







Cite this: *Nanoscale*, 2018, **10**, 6069

## Oxygen vacancy migration/diffusion induced synaptic plasticity in a single titanate nanobelt†

Ming Xiao,  ‡<sup>a,b,c</sup> Daozhi Shen,  ‡<sup>a,d,e</sup> Kevin P. Musselman,  <sup>a,b,c</sup>  
Walter W. Duley<sup>a,e</sup> and Y. Norman Zhou  \*<sup>a,b,c</sup>

Neuromorphic computational systems that emulate biological synapses in the human brain are fundamental in the development of artificial intelligence protocols beyond the standard von Neumann architecture. Such systems require new types of building blocks, such as memristors that access a quasi-continuous and wide range of conductive states, which is still an obstacle for the realization of high-efficiency and large-capacity learning in neuromorphic simulation. Here, we introduce hydrogen and sodium titanate nanobelts, the intermediate products of hydrothermal synthesis of TiO<sub>2</sub> nanobelts, to emulate the synaptic behavior. Devices incorporating a single titanate nanobelt demonstrate robust and reliable synaptic functions, including excitatory postsynaptic current, paired pulse facilitation, short term plasticity, potentiation and depression, as well as learning-forgetting behavior. In particular, the gradual modulation of conductive states in the single nanobelt device can be achieved by a large number of identical pulses. The mechanism for synaptic functionality of the titanate nanobelt device is attributed to the competition between an electric field driven migration of oxygen vacancies and a thermally induced spontaneous diffusion. These results provide insight into the potential use of titanate nanobelts in synaptic applications requiring continuously addressable states coupled with high processing efficiency.

Received 14th December 2017,  
Accepted 22nd February 2018

DOI: 10.1039/c7nr09335g

rs.c.li/nanoscale

### 1. Introduction

The ability of the human brain to perform high level parallel information processing while consuming ultralow power demonstrates that the brain has a superior architecture compared to that of less efficient conventional von Neumann systems where memory and processing units are physically separated.<sup>1,2</sup> The synapse is a basic element of the human brain and provides the functional interneuron link through which information is transmitted in the neural networks.<sup>3</sup> Synapses are considered to be the most important functional

units involving learning and memory response in the human brain.<sup>4,5</sup> Most notably, the synaptic transmission that relates the signal delivered from a presynaptic neuron to the resulting signal produced in a postsynaptic neuron is plastic and results in the potentiation and depression of short-term or long-term synaptic strength, enabling synaptic computation<sup>6,7</sup> or learning/memory<sup>8,9</sup> in the brain. A significant recent development is that memristive or resistive switching memory devices based on a variety of new materials, such as Ag<sub>2</sub>S, perovskite, organic PEDOT:PSS, Ag ion doped dielectric films<sup>10–15</sup> and field effect transistor (FET) devices,<sup>16–18</sup> have been used as building blocks with similar physical (*e.g.*, plastic) response to mimic biological synaptic functions. Two-terminal memristive devices, which have been used in imaging and facial recognition in neuromorphic computing,<sup>19–21</sup> have several advantages compared to the FET configuration. These include reduced complexity of the device structure and fabrication process, as well as lower energy consumption.<sup>22</sup> In practice, the conductance in a biological synapse is modulated by the exchange of Ca<sup>2+</sup> or Na<sup>+</sup> ions between the membrane and the synaptic junction in response to an action potential, whereas the conductance in a memristive device is controlled by the migration of metallic ions<sup>12,13</sup> or oxygen ions/vacancies<sup>23</sup> on application of a sweeping voltage or pulse. The use of memristors in neuromorphic computing applications requires a non-abrupt switching mechanism, *i.e.*, the continuous modulation

<sup>a</sup>Centre for Advanced Materials Joining, University of Waterloo, Waterloo, Ontario, N2L 3G1, Canada. E-mail: nzhou@uwaterloo.ca

<sup>b</sup>Waterloo Institute of Nanotechnology, University of Waterloo, Waterloo, Ontario, N2L 3G1, Canada

<sup>c</sup>Department of Mechanics and Mechatronics Engineering, University of Waterloo, Ontario, N2L 3G1 Waterloo, Canada

<sup>d</sup>Department of Mechanical Engineering, State Key Laboratory of Tribology, Tsinghua University, Beijing 100084, P. R. China

<sup>e</sup>Department of Physics and Astronomy, University of Waterloo, Waterloo, Ontario, N2L 3G1, Canada

† Electronic supplementary information (ESI) available: STEM characterization of titanate nanobelts, electrical performance of single nanobelt devices including electrical contact check and some synaptic performance. Material characterization of Na<sub>2</sub>Ti<sub>3</sub>O<sub>7</sub> nanobelts and their related synaptic performance. See DOI: 10.1039/c7nr09335g

‡ These two authors contribute equally to this work.

of conduction, analogous memory functionality and repeatable response.<sup>24</sup> This can be achieved by considering the internal dynamic of ion migration in a memristor device, the so-called second-order memristor,<sup>8,25</sup> and several intriguing synaptic functions such as synaptic metaplasticity<sup>26</sup> and triplet spike-timing dependent plasticity (STDP)<sup>27</sup> have been achieved based on the second-order memristive system. The availability of memristive devices with excellent performance, such as multi-conductive states and timing dependent plasticity, as required for the simulation of important synaptic responses such as learning, potentiation and depression, is therefore key to the development of neuromorphic systems.<sup>28</sup>

Nanowires or nanobelts are promising as building blocks for bottom-up fabrication in nanoelectronics. In particular, the study of artificial synaptic behavior based on individual 1D TiO<sub>2</sub> nanowire/nanobelt devices suggests that oxygen vacancies in the TiO<sub>2</sub>, and the migration of these vacancies under an applied electric field, are responsible for resistive switching and the accompanying synaptic response.<sup>29,30</sup> One of the most widely-used way to synthesize TiO<sub>2</sub> nanowires is the hydrothermal process.<sup>31</sup> In a typical hydrothermal synthesis of TiO<sub>2</sub> nanobelts from precursor nanoparticles such as commercial P25 nanoparticles, the first step involves the conversion of nanoparticles to sodium titanate nanobelts (Na<sub>2</sub>Ti<sub>3</sub>O<sub>7</sub>). These are then converted to hydrogen titanate (H<sub>2</sub>Ti<sub>3</sub>O<sub>7</sub>) in an ionic exchange process before finally becoming TiO<sub>2</sub> nanobelts during the annealing process.<sup>32</sup> Na<sub>2</sub>Ti<sub>3</sub>O<sub>7</sub> and H<sub>2</sub>Ti<sub>3</sub>O<sub>7</sub> nanobelts each have a layered crystalline structure consisting of octahedral [TiO<sub>6</sub>] units as in TiO<sub>2</sub> nanobelts,<sup>31,33</sup> and exhibit similar characteristics to TiO<sub>2</sub> nanobelts in applications such as gas sensing,<sup>31</sup> energy storage,<sup>34,35</sup> photocatalysis<sup>36,37</sup> and field emission.<sup>38,39</sup> This suggests that the presence and migration of oxygen vacancies is an important factor in all of these three materials.<sup>36,40,41</sup> However, the study of these intermediate products has largely been ignored for different applications, compared to the well-studied TiO<sub>2</sub> nanobelts. It would be more cost-effective and green if these intermediate nanobelts can be used in memristive synaptic devices since several more steps are needed to obtain TiO<sub>2</sub> nanobelts from these intermediate materials in the hydrothermal process. Therefore, a study of synaptic response in Na<sub>2</sub>Ti<sub>3</sub>O<sub>7</sub> and H<sub>2</sub>Ti<sub>3</sub>O<sub>7</sub> nanobelts is then of interest as this expands the research to titanates in addition to materials based on titanium metal oxide materials. It also enables a comparison of conduction mechanisms in all three materials in relation to their intrinsic properties.

In this paper, we examine the synaptic response of Na<sub>2</sub>Ti<sub>3</sub>O<sub>7</sub> and H<sub>2</sub>Ti<sub>3</sub>O<sub>7</sub> nanobelts, and the intermediate products of hydrothermally-synthesized TiO<sub>2</sub> nanobelts. Several synaptic functions, analogous to those seen in biological systems, are achieved in individual H<sub>2</sub>Ti<sub>3</sub>O<sub>7</sub> nanobelt devices. These functions include an excitatory postsynaptic current (EPSC), paired pulse facilitation (PPF), short-term plasticity, potentiation and depression as well as learning-forgetting response. The mechanism involved in the synaptic response can be associated with a competition between the migration of

oxygen vacancies driven by the electric field and subsequent spontaneous diffusion due to the resulting gradient in vacancy concentration. Individual Na<sub>2</sub>Ti<sub>3</sub>O<sub>7</sub> nanobelt devices also exhibit similar characteristics but carry smaller currents under similar excitation conditions.

## 2. Experiment and methods

### 2.1. Synthesis of sodium and hydrogen titanate nanobelts

Sodium and hydrogen titanate nanobelts were synthesized from the hydrothermal process of TiO<sub>2</sub> nanobelts as reported previously.<sup>32,42</sup> Typically, P25 (2 gram) Aeroxide™ (Sigma Aldrich, Canada) was dissolved in NaOH alkaline solution (60 mL, 10 mol) and then poured into a Teflon-lined stainless steel autoclave (125 mL, Parr Instruments). The autoclave was kept in a furnace at a temperature of 190 °C for 72 h. After cooling down the autoclave naturally, the suspended nanobelts were taken out and washed with ultrapure water. Sodium titanate (Na<sub>2</sub>Ti<sub>3</sub>O<sub>7</sub>) nanobelts were obtained after this process. Hydrogen titanate (H<sub>2</sub>Ti<sub>3</sub>O<sub>7</sub>) nanobelts could be obtained through an ionic exchange process for 12 h by transferring the Na<sub>2</sub>Ti<sub>3</sub>O<sub>7</sub> nanobelts into a beaker containing HCl solution (400 mL, 0.1 mol). The Na<sub>2</sub>Ti<sub>3</sub>O<sub>7</sub> and H<sub>2</sub>Ti<sub>3</sub>O<sub>7</sub> nanobelts were dried separately in a furnace at 80 °C for 8 h to obtain powders. Finally, nanobelts (0.5 mg) from powders were dispersed in acetone (20 mL) for device fabrication.

### 2.2. Device fabrication and characterization

The 4 μm gap Au electrodes were pre-fabricated on a SiO<sub>2</sub> wafer by standard photolithography and a lift-off process. The diluted nanobelt solution was drop-cast on the Au electrodes and dried in air. Devices with bridged nanobelts were examined with an Olympus BX51 optical microscope prior to electrical characterization. The electrical performance of single-nanobelt devices was evaluated using an Agilent B2985A Electrometer/High Resistance Meter and a homemade probe station. One end of the two electrodes was grounded and all the voltages were applied from the other end throughout the entire measurement.

### 2.3. Material characterization

Scanning electron microscopy (SEM) (ZEISS LEO 1550) and transmission electron microscopy (TEM) (JEOL 2010F) were used to examine the microstructure of the nanobelts and the configuration of the devices. The stoichiometry of the nanobelts was identified by X-ray diffraction (XRD, PANalytical X'pert PRO MRD). The bonding states of elemental sodium, titanium and oxygen in the nanobelts were examined by X-ray photoelectron spectroscopy (Thermo-VG Scientific ESCALab 250).

### 3. Results and discussion

#### 3.1. Materials characterization

Fig. 1 demonstrates the material characterization results of the as-synthesized  $\text{H}_2\text{Ti}_3\text{O}_7$  nanobelts. The nanobelts have a characteristic rectangular cross-section, as indicated by the inset magnified SEM images in Fig. 1a. The width of the nanobelt, as imaged in SEM and TEM scans, is typically 50–200 nm (Fig. 1a and b). A scanning TEM (STEM) image of a representative nanobelt and its corresponding line-scan obtained from electron energy loss spectroscopy indicate that the nanobelt has a width-to-height ratio of 4.2 : 1, consistent with a quasi-rectangular cross-section (Fig. S1, ESI<sup>†</sup>). This geometry ensures good electrical contact with the Au electrode. The high resolution TEM (HRTEM) image (Fig. 1c) of the nanobelt demonstrates a large concentration of void defects (indicated with arrows) with the measured interplanar spacing being  $\sim 0.20$  nm, corresponding to the (204) plane of the  $\text{H}_2\text{Ti}_3\text{O}_7$  crystal. These defects could be the existence of oxygen vacancies in the nanobelts, which is further confirmed by the Gaussian deconvolution peak of the O 1s spectrum centered at 532.5 eV (Fig. 1d and e). The overall stoichiometry of nanobelts is  $\text{H}_2\text{Ti}_3\text{O}_7$  as determined from the characteristic peaks by XRD measurement (Fig. 1f).

#### 3.2. Synaptic performance

**3.2.1. Excitatory postsynaptic current.** A schematic representation of the chemical pathways during transmission in a biological synapse is shown in Fig. 2a. The transmission of information between neurons involves the release of a neuro-

transmitter from the presynaptic terminal, followed by diffusion across the cleft and binding to postsynaptic receptors.<sup>17</sup> Neurotransmitters are contained in synaptic vesicles that cluster near the cell membrane in the axon terminal of the presynaptic neuron. Once an action potential propagates along the presynaptic axon and reaches the axon terminal, voltage-gated calcium ( $\text{Ca}^{2+}$ ) channels are activated and allow the flow of  $\text{Ca}^{2+}$  ions into the presynaptic terminal. This triggers fusion of the synaptic vesicle to the plasma membrane, resulting in the release of neurotransmitters in the synaptic cleft. These neurotransmitters dock with receptors on the postsynaptic neuron, triggering further molecular reactions that ultimately change the membrane potential of the postsynaptic neuron, generating a postsynaptic current.<sup>5</sup>

Fig. 2b is a schematic representation of an artificial synapse as it occurs in a single nanobelt device, and the inset SEM image demonstrates the device consisting of two Au electrodes separated by a 4  $\mu\text{m}$  gap bridged with a single  $\text{H}_2\text{Ti}_3\text{O}_7$  nanobelt. Under an external stimulus, spikes or action potentials in the presynaptic neuron (left electrode) are transmitted through the synapse (nanobelt) to the postsynaptic neuron (right electrode). This generates an excitatory postsynaptic current (EPSC). To simulate this excitatory response in our device, a series of 50 ms presynaptic pulses with amplitudes of 8, 10, 12, 15, 18 and 20 V were applied to one of the Au electrodes. These pulses were well separated in time ( $\sim 4$  s). The EPSC response of the device in this excitation regime is shown in Fig. 2c. It can be seen that the peak value of the EPSC increases from 0.53 nA to 4.45 nA as the amplitude of the presynaptic pulses increases from 8 V to 20 V. This type of EPSC

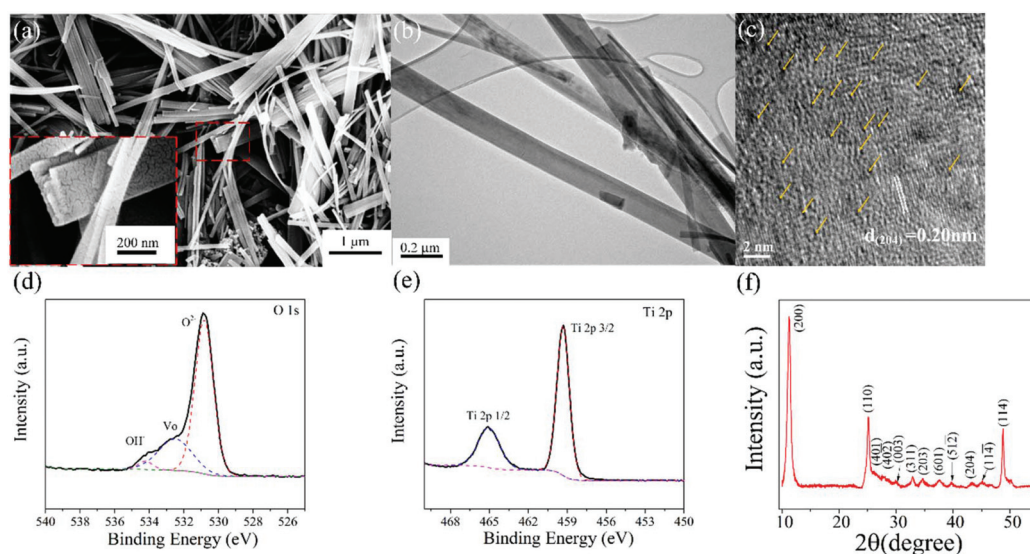


**Fig. 1** Material characterization of  $\text{H}_2\text{Ti}_3\text{O}_7$  nanobelts, (a) SEM image, inset shows a magnified view of the selected region. These images reveal that the nanobelts have a rectangular cross-section with a width of 50–200 nm and a length of several  $\mu\text{m}$ . (b) TEM image, (c) HRTEM image (arrows point out defects in the crystalline structure), (d) O 1s XPS spectra. The peak at 532.5 eV is attributed to oxygen vacancies (concentration  $\sim 26.33\%$ ), while the small shoulder at 534.2 eV is attributed to the  $\text{OH}^-$  group in the  $\text{H}_2\text{Ti}_3\text{O}_7$  nanobelts (concentration  $\sim 2.95\%$ ). The strongest peak arises from oxygen in the lattice. (e) Ti 2p XPS spectra, (f) XRD characterization of  $\text{H}_2\text{Ti}_3\text{O}_7$  nanobelts and their characteristic peaks indexed from the JCPDS database (no. 47-0561). Some characteristic peaks of  $\text{H}_2\text{Ti}_3\text{O}_7$  are indicated with arrows.

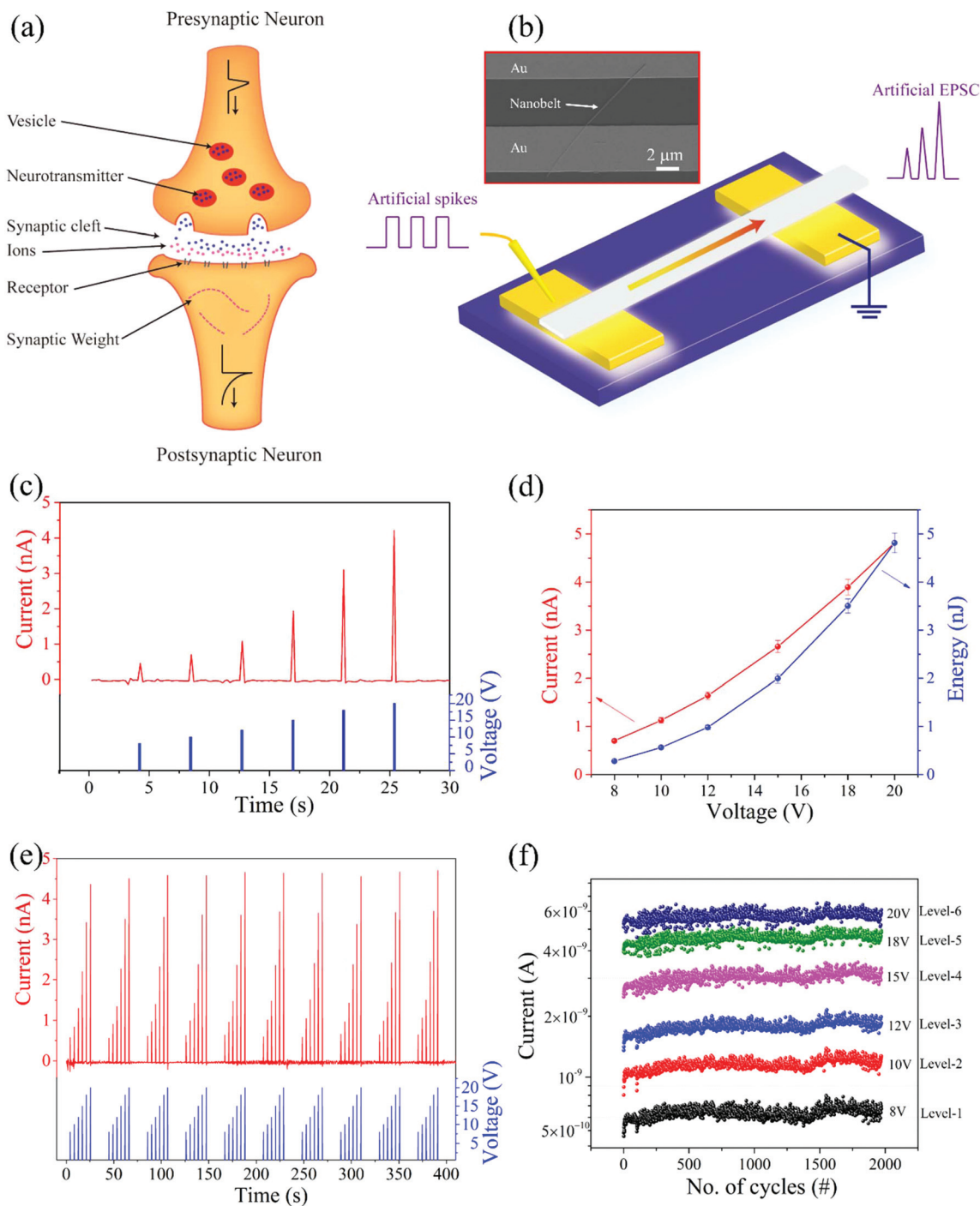


**Fig. 2** EPSC response, (a) schematic of a synapse, (b) schematic of the nanobelt device for the synaptic response study and SEM image of the nanobelt device, (c) EPSC performance for a series of 50 ms pulses with amplitudes 8, 10, 12, 15, 18 and 20 V, respectively, (d) summary of EPSCs and the corresponding calculated energy consumption, where the average currents and the corresponding standard deviation are calculated from the current responses over 2000 cycles as shown in (f), (e) EPSC during 10 cycles of EPSC excited as in (c), the interval period among adjacent cycles is 20 s. (f) EPSC evolution over 2000 cycles with pulse amplitudes as in (c).

response is similar to that observed in biological excitatory synapses.<sup>5</sup> The energy introduced into the device for a single pulse is  $E_{\text{con}} = I_{\text{avg}} \times t \times V$ , where  $I_{\text{avg}}$  is the average EPSC,  $t$  is the pulse duration and  $V$  is the pulse amplitude. The calculated values of  $E_{\text{con}}$  are shown in Fig. 2d. The smallest energy

consumption is estimated to be 212 pJ for the 8 V pulse. This power consumption could be further lowered by reducing the pulse duration to <50 ms.

After the spike, the current in the single nanobelt device assumes its baseline value. When the interval between pulses



is much longer than the pulse duration (*e.g.* 4–5 second interval *vs.* 50 ms duration), the EPSC induced by a given pulse does not affect the EPSC produced by the next spike.<sup>5,12</sup> Under these excitation conditions, the device exhibits a highly reproducible and controllable multilevel current response (Fig. 2e). The multilevel performance was tested up to 2000 cycles as shown in Fig. 2f. These data demonstrate a discrete, well separated current response, indicating that the multilevel conductive states of the single H<sub>2</sub>Ti<sub>3</sub>O<sub>7</sub> nanobelt device are highly robust.

**3.2.2. Short term plasticity.** Synaptic plasticity, defined as the change in the synaptic strength in response to external stimuli over time, is considered to be the foundation for learning and memory in the human brain.<sup>3</sup> In general, when two identical spikes arrive in rapid succession, the EPSC for the second spike is enhanced if the time interval between the spikes is short enough that carriers cannot relax to their initial equilibrium state between spikes, as illustrated schematically in Fig. 2b. This then leads to short-term synaptic enhancement or potentiation.<sup>43</sup> This response was successfully simulated in the present nanobelt device by applying two and ten consecutive identical +8 V pulses with an inter-pulse interval ranging from 100 to 3000 ms. Fig. 3a shows a typical example of short-term potentiation obtained at an inter-pulse interval of 500 ms. The amount of synaptic gained weight for two and ten equal pre-synaptic pulses was calculated as a function of the interval period as a way of mimicking neural paired-pulse facilitation (PPF) and post-tetanic potentiation (PTP) responses in a biological system. PPF measures the conductance increase that occurs on application of two consecutive presynaptic pulses, while PTP quantifies the increase in response for a

given number of spikes. The plasticity of the device can be described according to the PPF and PTP index models<sup>23,43</sup>

$$\text{PPF} = (I_2 - I_1)/I_1 \times 100\% \quad (1)$$

$$\text{PTP} = (I_{10} - I_1)/I_1 \times 100\% \quad (2)$$

In eqn (1) and (2),  $I_1$ ,  $I_2$  and  $I_{10}$  correspond to the current of the first, second and tenth pulse, respectively. From Fig. 3b and c, the amplitudes of the EPSC in the second (PPF) and tenth (PTP) pulses are 53% and 436% higher, respectively, compared to the EPSC from the first pulse at an inter-pulse interval of 100 ms. The high PTP index suggests the possibility that the nanobelt device may act as a dynamic high-pass filter.<sup>16</sup> The enhancement ratio is found to decrease with increasing inter-pulse time interval. This effect is also known as the spike rate-dependent plasticity (SRDP), whereby higher spike frequency leads to a larger increase in gained synaptic weight. Fitting of the PPF and PTP curves shows that the device plasticity decays exponentially *vs.* inter-pulse time interval.<sup>43</sup> In biological systems, a certain time interval is needed for the residual Ca<sup>2+</sup> concentration to relax to their equilibrium level after an action potential is terminated. When another identical stimulus follows shortly after the initial stimulus, a net increase in the synaptic response will occur, as in PPF. When many stimuli are applied and the inter-pulse interval is short, the synaptic transmission is progressively enhanced, as in PTP.

Fig. 3d–f show the enhancement in the current response during the application of 100 consecutive pulses. The duration, interval period and peak voltage per pulse are all seen to affect the overall current amplitude.<sup>14,50</sup> This potentiation be-

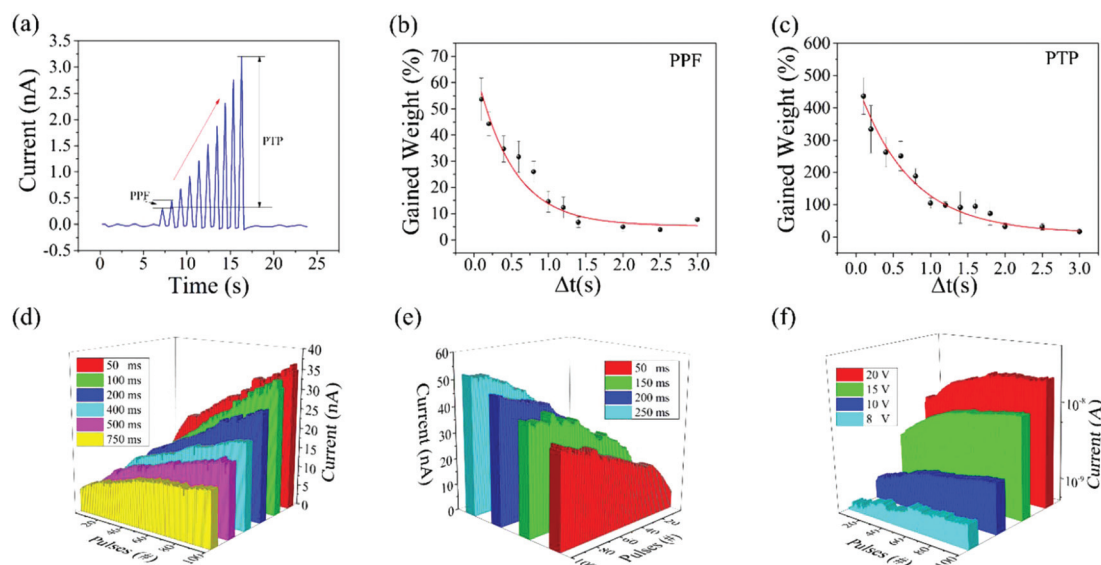


**Fig. 3** Short-term plasticity response. (a) Current enhancement for 10 consecutive, identical 8 V pulses. PPF and PTP are defined as shown, (b–c) relationship between gained weight (%) for PPF and PTP *vs.* the time interval between two consecutive pulses. The fitted exponential curves  $y = A_1 \times \exp(-x/t_1) + y_0$  are shown. For the PPF,  $A_1 = 0.625$ ,  $t_1 = 0.499$  s,  $y_0 = 0.053$  while for PTP,  $A_1 = 4.722$ ,  $t_1 = 0.707$  s,  $y_0 = 0.124$ , (d–f) accumulating current response on excitation with 100 identical consecutive pulses plotted *vs.* (d) time interval between pulses (50 ms duration, 20 V pulse), (e) pulse duration (50 ms interval, 20 V pulse), and (f) pulse amplitude (pulse duration and interval are 50 ms).

havior in the nanobelt device mimics the synaptic release of neurotransmitters in vesicles in response to a series of action potentials in which the frequency, duration, as well as amplitude of action potentials can stimulate a larger number of neurotransmitters, and thus a higher current response.<sup>17</sup> As can be seen in Fig. 3d–f, the accumulation of the current response does not scale linearly with an increase in the number of pulses. This suggests that more conductive states could be achieved using shorter pulse duration and lower pulse amplitude, as this would inhibit saturation, *i.e.*, slowing the increase in synaptic weight. By extending the number of identical low amplitude (10 V) pulses up to 1000 and using a variety of pulse durations, the current response can be gradually increased as shown in Fig. S2 (ESI<sup>†</sup>). A two orders of magnitude change in current accumulation was achieved through >1000 steps. It is apparent that the current continues to increase throughout the steps, but that the rate of increase is reduced as the number of pulses increases. More than 2000 modulation states can be achieved by applying a series of identical 50 and 100 ms, 10 V pulses, respectively (Fig. S3, ESI<sup>†</sup>). A gradual increase in current response is particularly important if the device is to mimic the analog nature of the synaptic weight change,<sup>44</sup> effective neural regulation and adaptive learning in neuromorphic computation.<sup>45</sup> With more resistance states, better learning efficiency and a greater capacity for an effective neuro-

morphic computing response are possible.<sup>28,45</sup> This indicates that H<sub>2</sub>Ti<sub>3</sub>O<sub>7</sub> nanobelts may be an attractive candidate for achieving high-efficiency learning in neuromorphic computing.

**3.2.3. Potentiation and depression.** In a system designed to implement artificial synapses, modulation of conductance can be used to emulate the effect of potentiation and depression on synaptic weight. This simulates the strengthening and weakening of pre- and post-synaptic neurons. To replicate this response, 100 consecutive +20 V, 100 ms, pulses followed by 100 consecutive –10 V, 100 ms, pulses were applied to the system. The resulting current response was read at 2 V and showed a reproducible potentiation and depression response, as summarized in Fig. 4a and b. The pulse peak current in this test is given in Fig. S4 (ESI<sup>†</sup>). The read-out current increases firstly in response to the positive input pulses, demonstrating potentiation. Subsequent negative pulses cause the current to decrease, resulting in depression of the response. The robustness of the potentiation and depression response was confirmed by a test involving 50 potentiation and 50 depression states for 5000 cycles (a total of 50 000 pulses) as shown in Fig. 4c and Fig. S5 in the ESI<sup>†</sup>. To test whether a larger number of potentiation and depression states are possible, the conductance was measured during application of >2000, +10 V/–6 V 100 ms pulse cycles (Fig. 4d). In the region of poten-

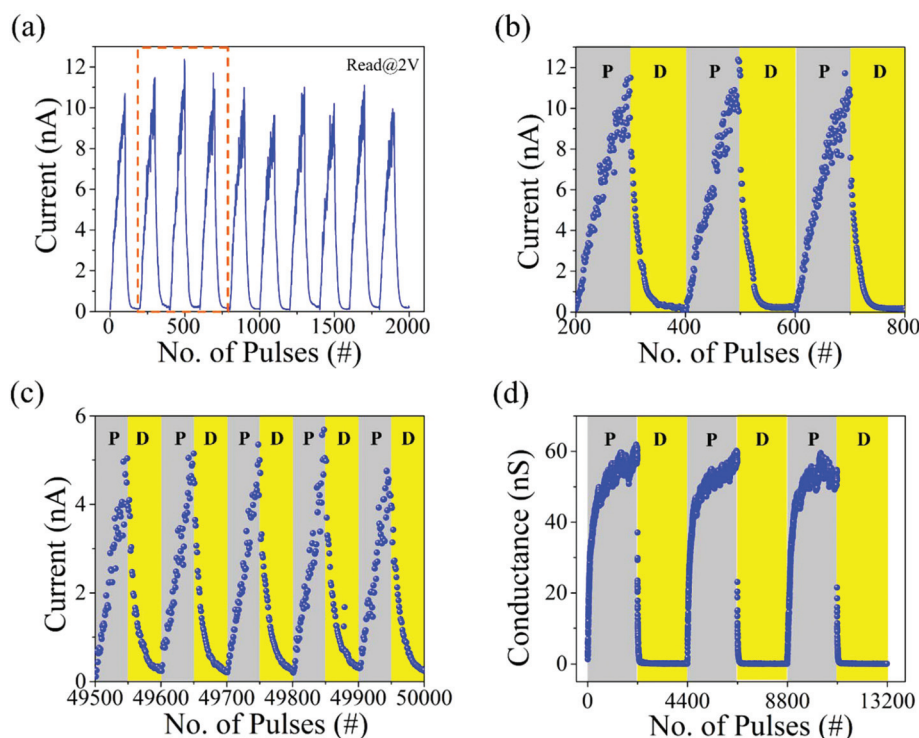


**Fig. 4** Potentiation and depression response. (a) 100, +20 V 100 ms pulses followed by 100, –10 V 100 ms pulses. The test was repeated for 10 cycles. Current was measured by a 2 V, 100 ms read pulse immediately after each potentiation and depression pulse. (b) Expanded view of the highlighted segment in (a). (c) Test over 50 000 pulses with 50 potentiation and 50 depression pulses as before. The response in the last 5 cycles is shown. (d) Test carried out to illustrate the large number of potentiation and depression states. Each cycle involved 2200, +10 V, 100 ms pulses followed by 2200, –6 V, 100 ms pulses. P and D indicate potentiation and depression, respectively.

tiation, the conductance of the device increases, and eventually becomes saturated. In the depression region, the conductance rapidly decreases during the first 300 pulses, and then remains essentially constant on the additional negative pulses. The latter effect might be due to the limited migration of oxygen vacancies on application of a low electric-field  $-6$  V pulse after the device has been returned to its initial state. The current response *vs.* time in this experiment is shown in Fig. S6 (ESI<sup>†</sup>). This suggests that a single nanobelt device can be used to combine a large number of potentiation and depression states in a simple structure. Moreover, the potentiation and depression response can also be generated in the  $\text{H}_2\text{Ti}_3\text{O}_7$  nanobelt device by sweeping voltages (Fig. 5). On the application of consecutive positive and negative sweeping voltages, the current amplitude first continuously increases (Fig. 5a) and then decreases (Fig. 5b). The cyclic current response *vs.* time and the corresponding conductance at the peak voltage are shown in Fig. 5c and d. It is also demonstrated in Fig. 4 that depression is faster than potentiation in the  $\text{H}_2\text{Ti}_3\text{O}_7$  nanobelt device. With higher amplitude negative pulses (*e.g.*,  $-15$  V and  $-20$  V rather than  $-10$  V), fewer negative pulses are sufficient to drive the current back to its original value (Fig. S7, ESI<sup>†</sup>). After the current returns to the baseline level, additional negative pulses contribute to the gene-

ration of higher current when the device is excited with opposite polarity pulses.<sup>28,46</sup>

**3.2.4. Learning and forgetting response.** We have also investigated the current accumulation and decay properties in these single  $\text{H}_2\text{Ti}_3\text{O}_7$  nanobelt devices to replicate the learning/forgetting response of human memory. Potentiation after application of a number of identical 500 ms pulses simulates the learning process, while forgetting can be simulated by following the subsequent decay of the current response. As before, the readout voltage was  $+2$  V. The resulting potentiation and decay curve is shown in Fig. 6a. When the exciting pulses are removed, the declining current is well described by an exponential decay, that is  $I = I_0 + Ae^{-t/\tau}$ , where  $I_0$  is the steady state current,  $t$  is time,  $A$  is a pre-factor, and  $\tau$  is a time constant, which indicates the forgetting rate (Fig. 6b). The spontaneous decay of current in the present device is analogous to the loss of memory or forgetting curve in a human brain.<sup>47,48</sup> We further studied the relaxation process of the device subject to a different number of applied pulses. It is shown in Fig. 6c that, by increasing the number of pulses to 400, the remaining normalized synaptic weight at 100 s increases from  $<3\%$  for 5 pulses to around 42%. Significantly, it is found that the time increases by a factor of 10 for the synaptic weight to decrease to 5% when the number of pulses is 400 ( $\sim 625$  s) compared to

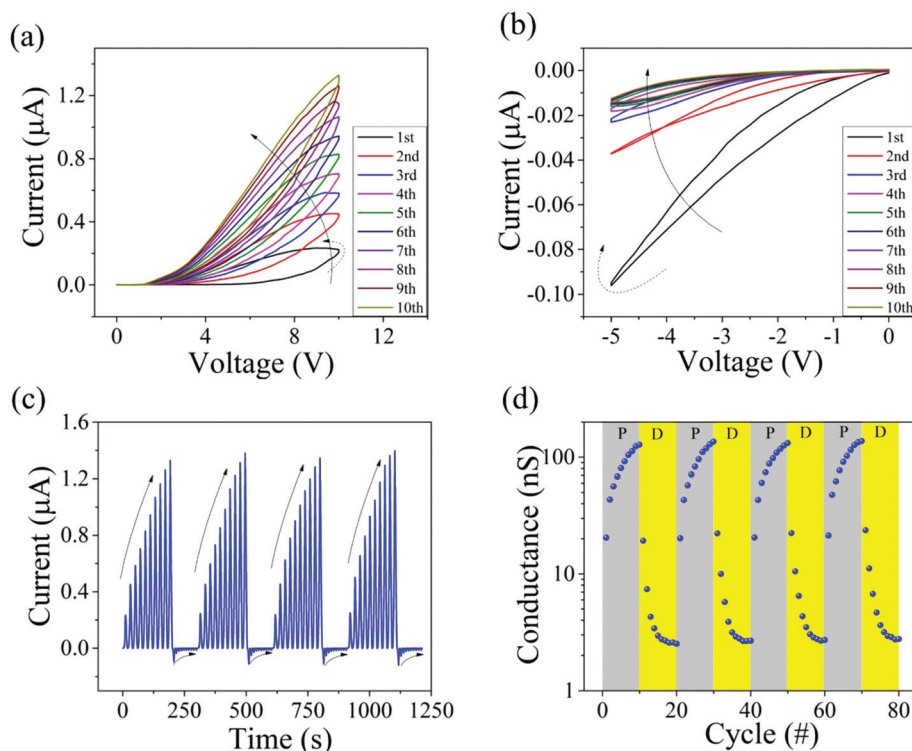


**Fig. 5** Nonlinear transmission characteristic of single positive and negative sweeping behavior. (a)  $I$ - $V$  characteristics of the single nanobelt device at positive sweeping voltages (0 to 10 V then back to 0 V). (b)  $I$ - $V$  characteristics of the single nanobelt device at negative sweeping voltages (0 to  $-5$  V then back to 0 V). (c) The curve of current response from (a) and (b) *versus* time. 4 cycles of potentiation and depression by sweeping voltage are demonstrated. (d) The conductance variation of the device with the sweeping cycles in (c). Reproducible potentiation (P) and depression (D) can be observed.

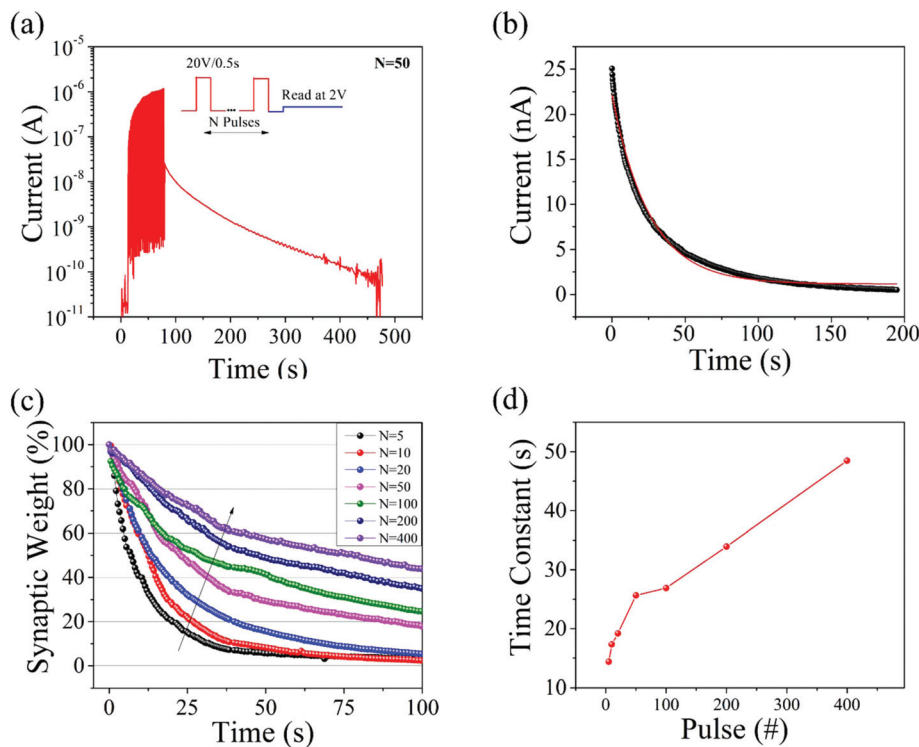


**Fig. 6** Learning and forgetting response and STP-to-LTP transition induced by repeated stimulation. (a) Learning and forgetting curve with 50, 500 ms, 20 V pulses. Current during relaxation was read at 2 V. (b) Current decay curve and its fit to the equation of  $I = I_0 + Ae^{-t/\tau}$ , where  $I_0 = 1.16$  nA,  $A = 20.9$  nA and  $\tau$  is 25.64 s. (c) Current decay behavior with the number of pulses up to 400 and (d) time constant summary up to 400 pulses.

that observed when the pulse number is 5 ( $\sim 59$  s). Meanwhile, the time constant increases with the increasing number of pulses as demonstrated in Fig. 6d. This suggests the potential for a transition from short-term potentiation (STP) to long-term potentiation (LTP) in the single nanobelt device by repeated stimulation.<sup>12</sup> This enhancement in stability induced by the repeated application of input pulses resembles the increase in synaptic strength through frequent stimulation by action potentials found in biological neural systems.<sup>12,49</sup>

Several important synaptic responses such as EPSC, SRDP and potentiation and depression responses, have also been measured in a single  $\text{Na}_2\text{Ti}_3\text{O}_7$  device (Fig. S8–S11, ESI<sup>†</sup>). In each case, the response is similar to that in the  $\text{H}_2\text{Ti}_3\text{O}_7$  nanobelt devices except that the current amplitudes are different, indicating the larger resistivity of the  $\text{Na}_2\text{Ti}_3\text{O}_7$  nanobelt. These results show that  $\text{H}_2\text{Ti}_3\text{O}_7$  and  $\text{Na}_2\text{Ti}_3\text{O}_7$  nanobelts, appearing as intermediate products in the formulation of  $\text{TiO}_2$  nanobelts by hydrothermal synthesis, are suitable for synaptic functionality emulation.

### 3.3. Kinetic mechanism

Similar to the analysis in the single  $\text{TiO}_2$  nanowire device,<sup>30,42</sup> it is suggested that the oxygen vacancies in the titanate nanobelts could be very important in the above mentioned synaptic performance. To examine the role of oxygen vacancies in the synaptic response of single  $\text{H}_2\text{Ti}_3\text{O}_7$  nanobelt devices, the temperature dependent time decay of the current (read at 2 V)

after excitation with 50 identical, +20 V, 500 ms pulses (same as Fig. 6a) is shown in Fig. 7. Fig. 7a indicates that the current decays more rapidly at higher temperature. This is consistent with the thermally activated diffusion of oxygen vacancies subject to an activation energy,  $E$ .<sup>60</sup> The process is described by eqn (3) where the time constant  $\tau$ , is temperature dependent,  $k$  is the Boltzmann constant,  $T$  is the absolute temperature and  $A_0$  is the pre-exponential rate constant,<sup>50</sup>

$$A_0 + \ln \frac{1}{\tau(T)} = \frac{E}{kT} \quad (3)$$

A plot of  $\ln(1/\tau(T))$  as a function of  $1000/T$  is shown in Fig. 7(b) and yields  $E = 0.33$  eV. This suggests a direct relationship between the oxygen vacancy diffusion and forgetting/relaxation response behavior in Fig. 6. Furthermore, the contact properties of the Au/nanobelt junction have been determined by examining its current response under a direct voltage sweep from  $-15$  V to  $15$  V. It was found that the  $I$ - $V$  curve is nearly symmetrical, implying that the device can be described by the model of back-to-back Schottky barriers in series with a resistor<sup>51,52</sup> (Fig. S12, ESI<sup>†</sup>). Under these conditions, oxygen vacancies would migrate towards one end of the Au/nanobelt interface under the applied electric field. This will lower the Schottky barrier at this interface, resulting in a rectifying-like  $I$ - $V$  curve.<sup>53</sup> To confirm this assumption, we measured the  $I$ - $V$  curves directly after sweeping from 0 to  $10$  V and found a positive rectification response. Similarly, a reverse



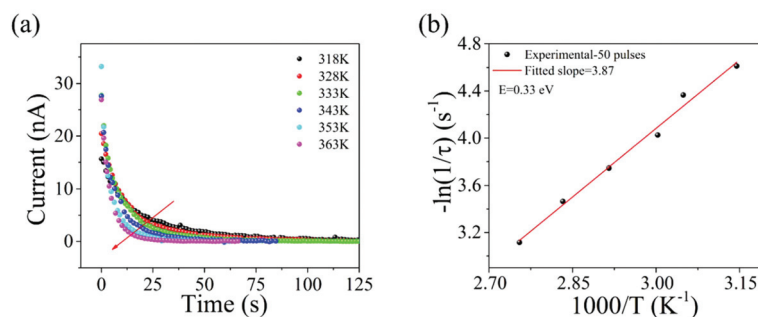


**Fig. 7** Synaptic mechanism study. (a) Temperature dependence of the current decay following excitation with 50 consecutive +20 V, 500 ms, pulses. The current was read at 2 V, (b) plot of  $\ln(1/\tau)$  vs.  $1000/T$  showing exponential dependence. The linear fit from eqn (3) is shown and implies that the diffusion activation energy is  $E = 0.33$  eV.

rectification characteristic is produced immediately after application of a 0 to  $-10$  V sweep voltage (Fig. S13, ESI†).

We have also investigated the temperature dependent current decay process in single  $\text{TiO}_2$  and  $\text{Na}_2\text{Ti}_3\text{O}_7$  nanobelt devices and have calculated the activation energies for diffusion using eqn (3). The resulting activation energies for  $\text{TiO}_2$  and  $\text{Na}_2\text{Ti}_3\text{O}_7$  nanobelt devices are 0.42 eV and 0.41 eV, respectively (Fig. S14, ESI†). Similar values of the activation energy in all three types of nanobelt devices suggest a common diffusion mechanism. The primary diffusion mechanism in all three types of nanobelt devices can then be attributed to oxygen vacancies although the diffusion of  $\text{H}^+$  and  $\text{Na}^+$  ions might play a limited role on  $\text{H}_2\text{Ti}_3\text{O}_7$  and  $\text{Na}_2\text{Ti}_3\text{O}_7$  nanobelts.

The low activation energies for diffusion in these three types of nanobelt devices compared to those found for many other oxides can be attributed to the geometrical effect of the nanowire/nanobelt structure. A recent theoretical report shows that a higher concentration of oxygen vacancies exists near and on the surface of ZnO nanowires. This facilitates the diffusion of oxygen vacancies in the nanowire structure compared to that occurring in bulk ZnO, because of the lower activation energy associated with surface defects.<sup>54</sup> This conclusion is supported by a recent study of oxygen diffusion in

sputtered  $\text{TiO}_2$  films, which shows that the activation energy for diffusion in the thin film is 1.05 eV.<sup>55</sup> Theoretical studies of migration of oxygen vacancies along different plane directions in bulk  $\text{TiO}_2$  also imply activation energies of 0.69–1.75 eV.<sup>56</sup> These values are consistent with the relatively low activation energies derived from our study of diffusion in single nanobelt devices.

The electrical characteristics of these nanobelt devices are then described by back-to-back Schottky barriers, whose properties are determined by the migration and diffusion of oxygen vacancies. In the absence of a bias, symmetrical Schottky barriers are formed at each junction between the nanobelt and an Au electrode (Fig. 8a). When an electric field is applied by biasing the device, oxygen vacancies distributed within the nanobelt migrate and accumulate at one of the Au/nanobelt interfaces, resulting in a reduction of the effective Schottky barrier.<sup>29,57–59</sup> This facilitates the injection of electrons from the Au electrode into the semiconductor nanobelt, enhancing the current flow in the forward direction.<sup>60</sup> The resistance of the device therefore decreases when oxygen vacancies accumulate at this end. Meanwhile, the corresponding increase in the density of defects at this end of the nanobelt gives rise to a concentration gradient. This gradient drives a diffusive flow of vacancies in an opposite direction to

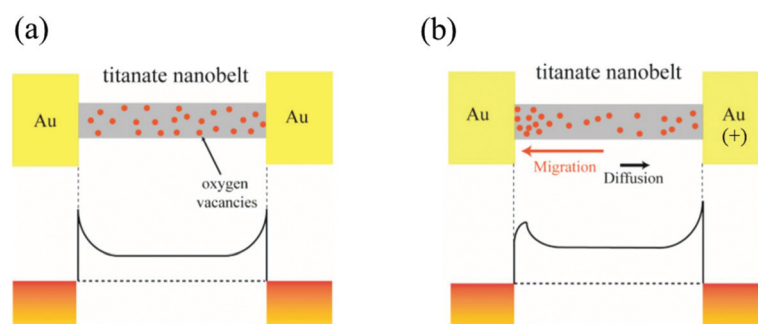


**Fig. 8** Schematic of the synaptic response mechanism. (a) In the initial state, oxygen vacancies are distributed randomly throughout the nanobelt, and a Schottky barrier is formed at each Au/nanobelt interface. (b) With applied positive electric field, the accumulation of oxygen vacancies at the left interface of the Au/nanobelt leads to a reduction in the strength of the Schottky barrier, increasing the conductivity of the device. Back diffusion of these defects in response to the concentration gradient would recover the Schottky barrier, leading to a decrease in the current response.

the electric field (Fig. 8b). As diffusion is thermally activated and has an activation energy,  $E$ , relaxation of the current following excitation in the forward direction is temperature dependent. The dynamic competition between these two mechanisms leads to different synaptic functions. As the number of pulses increases, these effects begin to cancel each other so that the current does not continue to grow at the same rate. The equilibrium established between migration and diffusion also results in current saturation as the number of pulses is increased. If the bias is reversed immediately after a positive voltage pulse, the electric field accelerates the flow of vacancies arising from diffusion and speeds up the overall depression response. This is also the reason for faster depression behavior than potentiation in the single nanobelt device. After a small number of negative voltage pulses, the device returns to its initial state and the Schottky barrier is re-established. Because of the identical nature of the Schottky barriers at each Au/nanobelt interface, the application of additional voltage pulses in the negative direction results in a similar response to that seen in the positive direction.

## 4. Conclusion

The synaptic properties of memristor devices based on single  $\text{H}_2\text{Ti}_3\text{O}_7$  and  $\text{Na}_2\text{Ti}_3\text{O}_7$  nanobelts have been investigated. Excellent synaptic functionalities, including the EPSC, short-term plasticity, potentiation and depression as well as learning-forgetting response, have been successfully demonstrated in a single nanobelt device. The gradual modulation in conductance with a large number of identical pulses is also realized. The synaptic responses are shown to derive from the modulation of a Schottky barrier at the electrode/nanobelt interface due to migration of oxygen vacancies driven by an applied electric field, and moderated by thermal diffusion in response to a gradient in defect concentration. Such intriguing properties of synaptic devices based on individual  $\text{H}_2\text{Ti}_3\text{O}_7$  and  $\text{Na}_2\text{Ti}_3\text{O}_7$  nanobelts, similar to the  $\text{TiO}_2$  nanobelts, not only show that these materials have a promising future in neuromorphic computing applications, but also suggest an alternative direction for material selection for synaptic functionality emulation study.

## Conflicts of interest

There are no conflicts to declare.

## Acknowledgements

This work was supported by the Natural Sciences and Engineering Research Council (NSERC). The financial support of the State Scholarship Fund of China (No. 201506160061) is greatly acknowledged. M. X. would like to thank Carmen Andrei from the Canadian Center for Electron Microscopy, McMaster University, for help with TEM.

## References

- 1 L. F. Abbott and W. G. Regehr, *Nature*, 2004, **431**, 796–803.
- 2 D. B. Strukov, *Nature*, 2011, **476**, 403–405.
- 3 G. W. Ng, *Brain-mind machinery: brain-inspired computing and mind opening*, World scientific, 2009.
- 4 V. M. Ho, J. A. Lee and K. C. Martin, *Science*, 2011, **334**, 623–628.
- 5 W. Xu, S. Y. Min, H. Hwang and T. W. Lee, *Sci. Adv.*, 2016, **2**, e1501326.
- 6 R. S. Zucker and W. G. Regehr, *Annu. Rev. Physiol.*, 2002, **64**, 355–405.
- 7 J. Wang, Y. Li, R. Liang, Y. Zhang, W. Mao, Y. Yang and T.-L. Ren, *IEEE Electron Device Lett.*, 2017, **38**, 1496–1499.
- 8 S. Kim, C. Du, P. Sheridan, W. Ma, S. Choi and W. D. Lu, *Nano Lett.*, 2015, **15**, 2203–2211.
- 9 H. Tian, W. Mi, X. F. Wang, H. Zhao, Q. Y. Xie, C. Li, Y. X. Li, Y. Yang and T. L. Ren, *Nano Lett.*, 2015, **15**, 8013–8019.
- 10 T. Hasegawa, T. Ohno, K. Terabe, T. Tsuruoka, T. Nakayama, J. K. Gimzewski and M. Aono, *Adv. Mater.*, 2010, **22**, 1831–1834.
- 11 Y. van de Burgt, E. Lubberman, E. J. Fuller, S. T. Keene, G. C. Faria, S. Agarwal, M. J. Marinella, A. Alec Talin and A. Salleo, *Nat. Mater.*, 2017, **16**, 414–418.
- 12 T. Ohno, T. Hasegawa, T. Tsuruoka, K. Terabe, J. K. Gimzewski and M. Aono, *Nat. Mater.*, 2011, **10**, 591–595.
- 13 Z. Wang, S. Joshi, S. E. Savel'ev, H. Jiang, R. Midya, P. Lin, M. Hu, N. Ge, J. P. Strachan, Z. Li, Q. Wu, M. Barnell, G. L. Li, H. L. Xin, R. S. Williams, Q. Xia and J. J. Yang, *Nat. Mater.*, 2017, **16**, 101–108.
- 14 Y. Yang, B. Chen and W. D. Lu, *Adv. Mater.*, 2015, **27**, 7720–7727.
- 15 W. Xu, H. Cho, Y. H. Kim, Y. T. Kim, C. Wolf, C. G. Park and T. W. Lee, *Adv. Mater.*, 2016, **28**, 5916–5922.
- 16 R. A. John, J. Ko, M. R. Kulkarni, N. Tiwari, N. A. Chien, N. G. Ing, W. L. Leong and N. Mathews, *Small*, 2017, **13**, 1701193.
- 17 A. J. Arnold, A. Razavieh, J. R. Nasr, D. S. Schulman, C. M. Eichfeld and S. Das, *ACS Nano*, 2017, **11**, 3110–3118.
- 18 S. Kim, B. Choi, M. Lim, J. Yoon, J. Lee, H. D. Kim and S. J. Choi, *ACS Nano*, 2017, **11**, 2814–2822.
- 19 M. Prezioso, F. Merrih-Bayat, B. D. Hoskins, G. C. Adam, K. K. Likharev and D. B. Strukov, *Nature*, 2015, **521**, 61–64.
- 20 P. Yao, H. Wu, B. Gao, S. B. Eryilmaz, X. Huang, W. Zhang, Q. Zhang, N. Deng, L. Shi, H. P. Wong and H. Qian, *Nat. Commun.*, 2017, **8**, 15199.
- 21 F. Alibart, E. Zamanidoost and D. B. Strukov, *Nat. Commun.*, 2013, **4**, 2072.
- 22 S. H. Jo, T. Chang, I. Ebong, B. B. Bhadviya, P. Mazumder and W. Lu, *Nano Lett.*, 2010, **10**, 1297–1301.
- 23 Y. F. Wang, Y. C. Lin, I. T. Wang, T. P. Lin and T. H. Hou, *Sci. Rep.*, 2015, **5**, 10150.
- 24 Z. Y. Wang, L. Y. Wang, M. Nagai, L. H. Xie, M. D. Yi and W. Huang, *Adv. Electron. Mater.*, 2017, **3**, 1600510.

- 25 C. Du, W. Ma, T. Chang, P. Sheridan and W. D. Lu, *Adv. Funct. Mater.*, 2015, **25**, 4290–4299.
- 26 Z. H. Tan, R. Yang, K. Terabe, X. B. Yin, X. D. Zhang and X. Guo, *Adv. Mater.*, 2016, **28**, 377–384.
- 27 R. Yang, H.-M. Huang, Q.-H. Hong, X.-B. Yin, Z.-H. Tan, T. Shi, Y.-X. Zhou, X.-S. Miao, X.-P. Wang, S.-B. Mi, C.-L. Jia and X. Guo, *Adv. Funct. Mater.*, 2018, **28**, 1704455.
- 28 H. Tian, W. Mi, H. Zhao, M. A. Mohammad, Y. Yang, P. W. Chiu and T. L. Ren, *Nanoscale*, 2017, **9**, 9275–9283.
- 29 D. S. Hong, Y. S. Chen, J. R. Sun and B. G. Shen, *Adv. Electron. Mater.*, 2016, **2**, 1500359.
- 30 C. J. O'Kelly, J. A. Fairfield, D. McCloskey, H. G. Manning, J. F. Donegan and J. J. Boland, *Adv. Electron. Mater.*, 2016, **2**, 1500458.
- 31 Y. M. Wang, G. J. Du, H. Liu, D. Liu, S. B. Qin, N. Wang, C. G. Hu, X. T. Tao, J. Jiao, J. Y. Wang and Z. L. Wang, *Adv. Funct. Mater.*, 2008, **18**, 1131–1137.
- 32 R. Liang, A. M. Hu, W. J. Li and Y. N. Zhou, *J. Nanopart. Res.*, 2013, **15**, 1990.
- 33 Z. Zhao, J. Tian, Y. Sang, A. Cabot and H. Liu, *Adv. Mater.*, 2015, **27**, 2557–2582.
- 34 A. Eguia-Barrio, E. Castillo-Martinez, M. Zarrabeitia, M. A. Munoz-Marquez, M. Casas-Cabanas and T. Rojo, *Phys. Chem. Chem. Phys.*, 2015, **17**, 6988–6994.
- 35 J. Y. Liao, D. Higgins, G. Lui, V. Chabot, X. Xiao and Z. Chen, *Nano Lett.*, 2013, **13**, 5467–5473.
- 36 A. Sarkar, K. Karmakar, A. K. Singh, K. Mandal and G. G. Khan, *Phys. Chem. Chem. Phys.*, 2016, **18**, 26900–26912.
- 37 W. J. Li, R. Liang, A. M. Hu, Z. H. Huang and Y. N. Zhou, *RSC Adv.*, 2014, **4**, 36959–36966.
- 38 I. Chakraborty, S. Chatterjee and P. Ayyub, *Appl. Phys. Lett.*, 2011, **99**, 143106.
- 39 X. Xu, C. Tang, H. Zeng, T. Zhai, S. Zhang, H. Zhao, Y. Bando and D. Golberg, *ACS Appl. Mater. Interfaces*, 2011, **3**, 1352–1358.
- 40 C. P. Saini, A. Barman, D. Das, B. Satpati, S. R. Bhattacharyya, D. Kanjilal, A. Ponomaryov, S. Zvyagin and A. Kanjilal, *J. Phys. Chem. C*, 2016, **121**, 278–283.
- 41 Q. Du and G. Lu, *J. Nanosci. Nanotechnol.*, 2015, **15**, 4385–4391.
- 42 L. C. Lin, L. Liu, K. Musselman, G. S. Zou, W. W. Duley and Y. N. Zhou, *Adv. Funct. Mater.*, 2016, **26**, 5979–5986.
- 43 G. Liu, C. Wang, W. B. Zhang, L. Pan, C. C. Zhang, X. Yang, F. Fan, Y. Chen and R. W. Li, *Adv. Electron. Mater.*, 2016, **2**, 1500298.
- 44 D. Kuzum, R. G. Jeyasingh, B. Lee and H. S. Wong, *Nano Lett.*, 2012, **12**, 2179–2186.
- 45 S. Yu, B. Gao, Z. Fang, H. Yu, J. Kang and H. S. Wong, *Adv. Mater.*, 2013, **25**, 1774–1779.
- 46 S. Kim, S. Choi and W. Lu, *ACS Nano*, 2014, **8**, 2369–2376.
- 47 Z. Q. Wang, H. Y. Xu, X. H. Li, H. Yu, Y. C. Liu and X. J. Zhu, *Adv. Funct. Mater.*, 2012, **22**, 2759–2765.
- 48 X. B. Yin, R. Yang, K. H. Xue, Z. H. Tan, X. D. Zhang, X. S. Miao and X. Guo, *Phys. Chem. Chem. Phys.*, 2016, **18**, 31796–31802.
- 49 B. J. Murdoch, D. G. McCulloch, R. Ganesan, D. R. McKenzie, M. M. M. Bilek and J. G. Partridge, *Appl. Phys. Lett.*, 2016, **108**, 143504.
- 50 H. Tian, Q. Guo, Y. Xie, H. Zhao, C. Li, J. J. Cha, F. Xia and H. Wang, *Adv. Mater.*, 2016, **28**, 4991–4997.
- 51 Y. F. Lin and W. B. Jian, *Nano Lett.*, 2008, **8**, 3146–3150.
- 52 Z. Y. Zhang, C. H. Jin, X. L. Liang, Q. Chen and L. M. Peng, *Appl. Phys. Lett.*, 2006, **88**, 073102.
- 53 J. J. Yang, M. D. Pickett, X. Li, D. A. Ohlberg, D. R. Stewart and R. S. Williams, *Nat. Nanotechnol.*, 2008, **3**, 429–433.
- 54 B. Deng, A. Luisa da Rosa, T. Frauenheim, J. P. Xiao, X. Q. Shi, R. Q. Zhang and M. A. Van Hove, *Nanoscale*, 2014, **6**, 11882–11886.
- 55 G. G. Marmitt, S. K. Nandi, D. K. Venkatachalam, R. G. Elliman, M. Vos and P. L. Grande, *Thin Solid Films*, 2017, **629**, 97–102.
- 56 H. Iddir, S. Ögüt, P. Zapol and N. D. Browning, *Phys. Rev. B: Condens. Matter*, 2007, **75**, 073203.
- 57 R. Yang, K. Terabe, G. Liu, T. Tsuruoka, T. Hasegawa, J. K. Gimzewski and M. Aono, *ACS Nano*, 2012, **6**, 9515–9521.
- 58 J. J. Yang, J. P. Strachan, F. Miao, M. X. Zhang, M. D. Pickett, W. Yi, D. A. A. Ohlberg, G. Medeiros-Ribeiro and R. S. Williams, *Appl. Phys. A: Mater. Sci. Process.*, 2011, **102**, 785–789.
- 59 C. O'Kelly, J. A. Fairfield and J. J. Boland, *ACS Nano*, 2014, **8**, 11724–11729.
- 60 J. M. Shannon, *Solid-State Electron.*, 1976, **19**, 537–543.